

Gap solitons in elongated geometries: the one-dimensional Gross-Pitaevskii equation and beyond

A. Muñoz Mateo* and V. Delgado†

*Departamento de Física Fundamental II, Facultad de Física,
Universidad de La Laguna, 38206 La Laguna, Tenerife, Spain*

Boris A. Malomed‡

*Department of Physica Electronics, School of Electrical Engineering,
Faculty of Engineering, Tel Aviv University, Tel Aviv 69978, Israel*

(Dated: 15 February 2011)

We report results of a systematic analysis of matter-wave gap solitons (GSs) in the 3D self-repulsive BEC (Bose-Einstein condensate), loaded into a combination of a cigar-shaped trap and axial OL (optical-lattice) potential. Basic cases of the strong, intermediate, and weak radial (transverse) confinement are considered, as well as settings with shallow and deep OL potentials. Only in the case of the shallow lattice combined with the tight radial confinement, which actually has little relevance to realistic experimental conditions, the usual 1D cubic Gross-Pitaevskii equation (GPE) furnishes a sufficiently accurate description of GSs. However, the effective 1D equation with the nonpolynomial nonlinearity, derived in Ref. [17], provides for quite an accurate approximation for the GSs in all cases, including the situation with the weak transverse confinement, when the soliton's shape includes a considerable contribution from higher-order transverse modes, in addition to the usual ground-state wave function of the respective harmonic oscillator. Both fundamental GSs and their multi-peak bound states are considered. The stability is analyzed by means of systematic simulations. It is concluded that almost all the fundamental GSs are stable, while their bound states may be stable if the underlying OL potential is deep enough.

PACS numbers: 03.75.Lm; 05.45.Yv

I. INTRODUCTION

Matter-wave gap solitons (GSs) are localized modes that can be created in elongated Bose-Einstein condensates (BECs) loaded into one-dimensional (1D) optical-lattice (OL) potentials, with the intrinsic nonlinearity induced by repulsive interactions between atoms. GSs have been the topic of a large number of original works. Results produced by these studies were summarized in several reviews [1–5]. Within the framework of the mean-field approximation, the description of matter-wave patterns is based on the Gross-Pitaevskii equation (GPE) for the macroscopic wave function ψ [6],

$$i\hbar \frac{\partial \psi}{\partial t} = \left(-\frac{\hbar^2}{2M} \nabla^2 + V_{\perp}(\mathbf{r}_{\perp}) + V_z(z) + gN |\psi|^2 \right) \psi, \quad (1)$$

that has proven to be very successful in reproducing experimental results for the zero-temperature BEC (for instance, for multiple vortices, as shown in detail in Refs. [7, 8]). In this equation, M is the atomic mass, the norm of the wave function ψ is unity, N is the number of atoms, and $g = 4\pi\hbar^2 a/M$ is the interaction strength with a being the s -wave scattering length. In this work, we consider only repulsive interactions, i.e., $a > 0$. Further, $V_{\perp}(\mathbf{r}_{\perp}) = (1/2)M\omega_{\perp}^2 r_{\perp}^2$ is the radial-confinement potential, and $V_z(z)$ is the axial potential, which may include the axial harmonic trap and the 1D OL, with depth V_0 and period d :

$$V_z(z) = (1/2)M\omega_z^2 z^2 + V_0 \sin^2(\pi z/d). \quad (2)$$

The energy scale in the underlying (no-interaction) linear problem is set by the OL's recoil energy, $E_R = \hbar^2 \pi^2 / 2Md^2$.

Most commonly, theoretical studies of GSs in elongated geometries are carried out in terms of the 1D GPE [1, 2, 9–13],

$$i\hbar \frac{\partial \phi}{\partial t} = -\frac{\hbar^2}{2M} \frac{\partial^2 \phi}{\partial z^2} + V_z(z)\phi + g_{1D}N |\phi|^2 \phi, \quad (3)$$

where $g_{1D} = 2a\hbar\omega_{\perp}$. This is an effective evolution equation for the axial dynamics—described by the 1D wave function $\phi(z, t)$ —which can be derived from the full three-dimensional GPE after averaging out the radial degrees of freedom under the assumption that the radial confinement is so tight that the transverse dynamics is frozen to zero-point oscillations. These conditions, however, are not easy to realize using typical experimental parameters [2], and when such conditions are not met the transverse excitations can no longer be neglected, making an essentially 3D analysis necessary. In this work, we aim to investigate different physically relevant regimes and capture 3D effects in the generation and stability of matter-wave GSs in elongated BECs. This analysis should make it possible to determine the range of validity of the 1D GPE for the description of the GSs under typical experimental conditions, as well as characteristic features of the fundamental and higher-order GSs in realistic situations.

In principle, when the transverse excitations are relevant, Eq. (3) fails and one has to resort to the full 3D GPE (1), as recently done in Ref. [14], or, alternatively, use

extended 1D models that, within the framework of certain assumptions, take into account effects of higher-order radial modes on the axial dynamics of the condensate, leading to effective 1D equations with the cubic-quintic [15] or nonpolynomial [16, 17] nonlinearities. In this work, we will consider both the full 3D GPE and the effective 1D model with a nonpolynomial nonlinearity, which was derived, for the case of the self-repulsive nonlinearity, in Ref. [17]. The latter one, which represents a simple generalization of the usual 1D GPE, that reduces to Eq. (3) in the appropriate limit, has demonstrated an excellent quantitative agreement with experimental observations [18–21] (chiefly, for delocalized dark solitons, which are natural patterns in the case of the self-repulsion; however, the comparison was not reported before for localized GS modes). We will demonstrate that, while the range of applicability of the 1D GPE (3) is severely limited in realistic situations, the above-mentioned generalization gives a good description of stationary matter-wave GSs in virtually all cases of practical interest.

The paper is organized as follows. The model is formulated in Section II, where we also recapitulate the derivation of the effective nonpolynomial 1D equation, following the lines of Ref. [17], as this derivation is essential for the presentation of the results for the GSs. Main findings are collected in Sections III, where families of GS solutions are reported in several physically relevant regimes: for the strong, intermediate, and weak transverse confinement, and shallow or deep OL potential. Both fundamental GSs and their multi-peak bound states are considered. Only in the case of the tight confinement combined with a shallow OL the ordinary 1D GPE provides for a sufficiently accurate description of the GSs, in comparison with results of full 3D computations. On the other hand, the effective nonpolynomial 1D equation provides for good accuracy in all cases, for the fundamental solitons and their bound states alike. The stability of the GSs is studied in Section IV, by means of systematic simulations of the evolution of perturbed solitons. The conclusion is that the fundamental GSs are stable (except for in a narrow region close to the upper edge of the bandgaps), even in the case of the strong deviation from the usual 1D description. Multi-soliton bound states are stable if the OL potential is deep enough. Conclusions following from results of this work, including applicability limits for the mean-field approximation and 1D approximations, are formulated in Section V.

II. THE MODEL

The model that was developed in Ref. [17] for the BEC in the absence of OL potentials resorted to the *adiabatic approximation*, to neglect correlations between the transverse and axial motions. This approximation assumes that the axial density varies slowly enough to allow the trans-

verse wave function follow these slow variations. Because the OL imposes a new spatial scale, which may be more restrictive, it is necessary to find out if the adiabatic approximation remains valid in the presence of the OL. To this end, we will now briefly recapitulate the derivation of the effective 1D equation based on this approximation.

The starting point is the ansatz based on the factorized 3D wave function,

$$\psi(\mathbf{r}, t) = \varphi(\mathbf{r}_\perp; n_1(z, t))\phi(z, t), \quad (4)$$

with $n_1(z, t)$ being the local condensate density per unit length characterizing the axial configuration:

$$n_1(z, t) \equiv N \int d^2\mathbf{r}_\perp |\psi(\mathbf{r}_\perp, z, t)|^2 = N |\phi(z, t)|^2. \quad (5)$$

To derive Eq. (5), we have assumed that the transverse wave function φ is normalized to unity. Next, the substitution of Eq. (4) into the 3D equation (1) leads to

$$\begin{aligned} & \left(i\hbar \frac{\partial \phi}{\partial t} + \frac{\hbar^2}{2M} \frac{\partial^2 \phi}{\partial z^2} - V_z \phi \right) \varphi = \\ & \left(-\frac{\hbar^2}{2M} \nabla_\perp^2 \varphi - \frac{\hbar^2}{2M} \frac{\partial^2 \varphi}{\partial z^2} + V_\perp \varphi + gn_1 |\varphi|^2 \right) \phi - \frac{\hbar^2}{M} \frac{\partial \varphi}{\partial z} \frac{\partial \phi}{\partial z}. \end{aligned} \quad (6)$$

Because of the very different time scales of the axial and radial motions, it is natural to assume that the slow axial dynamics may be accurately described by averaging Eq. (6) over the fast (radial) degrees of freedom. Doing this, one obtains

$$\begin{aligned} i\hbar \frac{\partial \phi}{\partial t} &= -\frac{\hbar^2}{2M} \frac{\partial^2 \phi}{\partial z^2} + V_z \phi + \mu_\perp \phi - \frac{\hbar^2}{M} \left(\int d^2\mathbf{r}_\perp \varphi^* \frac{\partial \varphi}{\partial z} \right) \frac{\partial \phi}{\partial z}, \\ \mu_\perp(n_1) &\equiv \int d^2\mathbf{r}_\perp \varphi^* \left(-\frac{\hbar^2}{2M} \nabla_\perp^2 - \frac{\hbar^2}{2M} \frac{\partial^2}{\partial z^2} + V_\perp + gn_1 |\varphi|^2 \right) \varphi. \end{aligned} \quad (7)$$

Since $n_1(z, t)$ enters the last term of Eq. (8) merely as an external parameter, it is clear that, whenever the axial kinetic energy associated with the transverse wave function may be neglected, i.e.,

$$\begin{aligned} K_z[\varphi] &\equiv \int d^2\mathbf{r}_\perp \varphi^* \left(-\frac{\hbar^2}{2M} \frac{\partial^2}{\partial z^2} \right) \varphi \\ &\ll \int d^2\mathbf{r}_\perp \varphi^* \left(-\frac{\hbar^2}{2M} \nabla_\perp^2 + V_\perp(\mathbf{r}_\perp) + gn_1 |\varphi|^2 \right) \varphi, \end{aligned} \quad (9)$$

the radial dynamics decouples and $\mu_\perp(n_1)$ can be determined without the knowledge of the axial wave function. Actually, the right-hand side of Eq. (9) is the chemical potential of an axially homogeneous condensate characterized by the density per unit length n_1 and wave function φ . For a sufficiently small value of the linear density ($an_1 \ll 1$), the chemical potential of the lowest-energy state of this homogeneous condensate can be readily obtained perturbatively. In this case, to the lowest order, $\varphi(\mathbf{r}_\perp)$ is given by

the Gaussian wave function of the ground state of the radial harmonic oscillator, the corresponding chemical potential being $\hbar\omega_\perp(1 + 2an_1)$. As the linear density increases, more radial modes become excited, and, in generally, the ground state of the corresponding homogeneous condensate involves many harmonic-oscillator modes.

In previous works, it was shown, using different approaches, that also in this case an analytical solution can be constructed [17]. In particular, by using a variational approach based on the direct minimization of the chemical-potential functional, it was shown that for any (dimensionless) linear density an_1 a very accurate estimate for the chemical potential of the ground state is given by $\hbar\omega_\perp\sqrt{1 + 4an_1}$ [22]. This expression can be easily extended to incorporate the case in which the condensate contains an axisymmetric vortex [17] (see also Ref. [23], where the intrinsic vorticity was included into the derivation of the 1D nonpolynomial nonlinear Schrödinger equation in the case of the self-attraction); however, in this work we restrict the consideration to zero vorticity. Using Eq. (9), we see that a sufficient condition for the second derivative in z appearing in Eq. (8) to be negligible is

$$K_z[\varphi] \ll \hbar\omega_\perp\sqrt{1 + 4an_1}. \quad (10)$$

Taking into account an estimate, $K_z[\varphi] \sim \hbar^2/2M\Delta_z^2$, where Δ_z is the characteristic length scale in the axial direction, Eq. (10) can be rewritten as

$$\frac{\hbar^2}{2M\Delta_z^2} \ll \hbar\omega_\perp\sqrt{1 + 4an_1}. \quad (11)$$

When this condition holds, $\mu_\perp(n_1)$ coincides, to a good approximation, with the transverse local chemical potential of the stationary radial GPE,

$$\left(-\frac{\hbar^2}{2M}\nabla_\perp^2 + V_\perp(\mathbf{r}_\perp) + gn_1|\varphi|^2\right)\varphi = \mu_\perp(n_1)\varphi, \quad (12)$$

and is given by

$$\mu_\perp(n_1) = \hbar\omega_\perp\sqrt{1 + 4an_1}. \quad (13)$$

Finally, substituting Eqs. (13) and (5) into Eq. (7) and taking into account that φ is a real normalized wave function (which implies the vanishing of the integral in the last term) we arrive at the following effective 1D equation to govern the slow axial dynamics of the condensate:

$$i\hbar\frac{\partial\phi}{\partial t} = -\frac{\hbar^2}{2M}\frac{\partial^2\phi}{\partial z^2} + V_z(z)\phi + \hbar\omega_\perp\sqrt{1 + 4aN}|\phi|^2\phi. \quad (14)$$

We note that the contribution from interatomic interactions enters the above equation through term $\hbar\omega_\perp\left(\sqrt{1 + 4aN}|\phi|^2 - 1\right)\phi$, which vanishes for $N \rightarrow 0$. Thus, Eq. (14) incorporates the energy shift $\hbar\omega_\perp$, which is irrelevant for the dynamics but simplifies the form of the equation and makes the global chemical potential, that follows from this effective 1D equation, exactly coinciding with the corresponding 3D result.

The above derivation demonstrates that the validity of Eq. (14) relies on two conditions:

(i) The typical time scale Δ_t of the axial motion must be much larger than the typical time scale of the radial motion ($\sim \omega_\perp^{-1}$);

(ii) The axial kinetic energy, $K_z[\varphi]$, associated with the transverse wave function must be negligible.

The former requirement is necessary to allow the radial wave function to adiabatically follow the axial dynamics. While the specific temporal scale Δ_t depends on the particular initial conditions, typically, in the presence of an OL, the fulfillment of this condition gets more difficult as the lattice period d decreases, or the linear density an_1 increases. In particular, a sufficient condition for the validity of the adiabatic approximation is: $d \gg a_\perp$, $an_1 \ll 1$, with $a_\perp \equiv \sqrt{\hbar/M\omega_\perp}$ being the radial harmonic-oscillator length. Nevertheless, such a constraint, which is hard to satisfy in realistic situations, is not a necessary condition. Actually, for stationary states $\Delta_t \rightarrow \infty$ and condition (i) always holds. In the present work we are interested in this case, which is the most relevant one to seek for matter-wave GSs.

A sufficient condition for the fulfillment of condition (ii) is given by the inequality (11). In the presence of an OL, the characteristic length scale Δ_z is typically on the order of the lattice period d , hence Eq. (11) becomes

$$E_R \ll \hbar\omega_\perp\sqrt{1 + 4an_1}, \quad (15)$$

where E_R is the corresponding recoil energy. We will demonstrate that this condition is well satisfied for stationary GSs in most cases of interest.

It is clear that, when the linear density is small enough ($an_1 \ll 1$), Eq. (14), which exhibits the nonpolynomial nonlinearity, reduces to the usual 1D GPE (3) with the cubic nonlinearity. This is the quasi-1D mean-field regime, which corresponds to condensates whose radial state, as given by a solution to Eq. (12), may be well approximated by the Gaussian ground state of the corresponding harmonic oscillator [17, 24]. Thus, Eq. (14) represents an extension of the 1D GPE for condensates with larger linear densities or, equivalently, larger mean-field interaction energies. In such condensates, the radial ground state satisfying Eq. (12) is, in general, a linear combination of many harmonic-oscillator modes (a similar situation takes place in the derivation of the effective 1D equation for fermionic gases by means of the density-functional approach [25]).

Inspection of Eqs. (1) or (14) demonstrates that the dynamical problem is fully controlled by four dimensionless parameters, which may be defined as

$$\frac{E_R}{\hbar\omega_\perp}, \frac{V_0}{E_R}, \frac{\omega_z}{\omega_\perp}, \frac{Na}{a_\perp}. \quad (16)$$

As said above, the recoil energy E_R sets the energy scale of the underlying linear problem, while the nonlinear coupling constant Na/a_\perp determines the order of magnitude of the mean-field interaction energy in units of the radial

quantum $\hbar\omega_{\perp}$. Note that the dimensionless linear density an_1 is proportional to Na/a_{\perp} .

In this work, we assume the axial confinement to be so weak that the corresponding harmonic-oscillator length, $a_z \equiv \sqrt{\hbar/M\omega_z}$, is much larger than the lattice period d . Under these conditions, it is safe to neglect the modulation induced in the condensate density by the axial harmonic trap and set $\omega_z = 0$, so that we are left with a uniform 1D lattice potential acting along the axial direction.

III. MATTER-WAVE GAP SOLITONS IN DIFFERENT PHYSICAL REGIMES

The stationary solutions of the 3D GPE are wave functions of the form $\psi(\mathbf{r}, t) = \psi_0(\mathbf{r}) \exp(-i\mu t)$, with ψ_0 obeying the time-independent GPE,

$$\mu\psi_0 = \left(-\frac{\hbar^2}{2M} \nabla^2 + V_{\perp}(\mathbf{r}_{\perp}) + V_z(z) + gN |\psi_0|^2 \right) \psi_0, \quad (17)$$

where μ is the chemical potential. When Eq. (14) is applicable, one can instead generate the stationary axial wave function $\phi_0(z)$ by solving the effective 1D equation,

$$\mu\phi_0 = \left(-\frac{\hbar^2}{2M} \frac{\partial^2}{\partial z^2} + V_z(z) + \hbar\omega_{\perp} \sqrt{1 + 4aN |\phi_0|^2} \right) \phi_0, \quad (18)$$

which, in the limit of $an_1 \ll 1$, reduces to the time-independent version of the usual 1D GPE (3):

$$\mu\phi_0 = \left(-\frac{\hbar^2}{2M} \frac{\partial^2}{\partial z^2} + V_z(z) + g_{1D}N |\phi_0|^2 + \hbar\omega_{\perp} \right) \phi_0. \quad (19)$$

Matter-wave GSs are characterized by the chemical potential lying in a bandgap of the energy spectrum of the underlying linear system. To construct solutions for realistic 3D matter-wave GSs in the effectively 1D geometry, we looked for numerical solutions to Eqs. (17) and (18) in different physically relevant regimes, and compared the obtained results with those produced by the usual 1D GPE (19) to determine to what extent 3D contributions are relevant. In particular, the comparison allows us to estimate the accuracy and range of applicability of the effective 1D equations (18) and (19).

Experimentally relevant values for the OL period d range from 0.4 to 1.6 μm [2], which implies that, for the condensate of ^{87}Rb , $E_R/2\pi\hbar$ ranges from 3.6 kHz to 220 Hz. Taking into account that, typically, $\omega_{\perp}/2\pi \lesssim 1$ kHz, we conclude that $E_R/\hbar\omega_{\perp} \gtrsim 1/4$. On the other hand, for the condensate of ^{23}Na one has $E_R/\hbar\omega_{\perp} \gtrsim 1$ [26], therefore in this case the GS energy is sufficiently large to excite higher modes of the radial confinement, which makes 3D contributions always relevant. Since the ^{87}Rb condensate is most relevant for the experimental realization of GSs in the quasi-1D setting [27, 28], in what follows below we use particular parameters of this condensate to illustrate our results. Nevertheless, the results of the present work, which

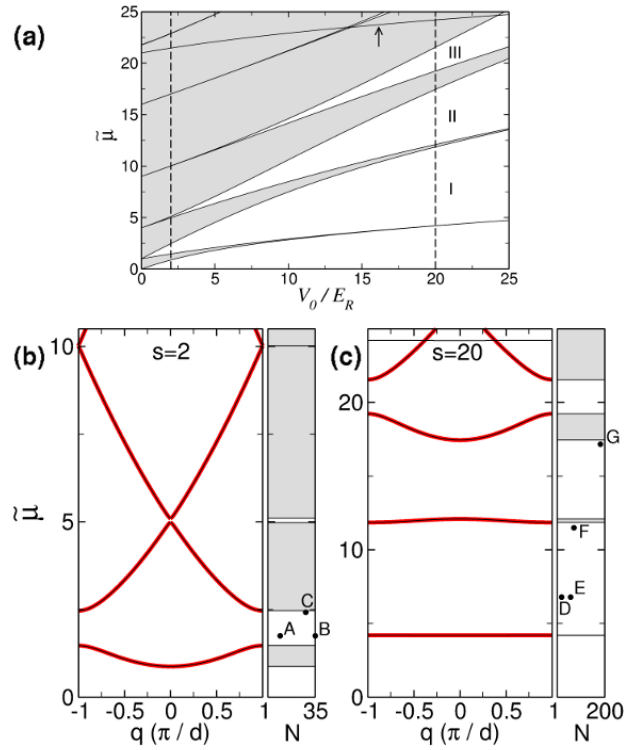


FIG. 1: (Color online). (a) Band-gap structure of a noninteracting 3D BEC with $E_R/\hbar\omega_{\perp} = 1/10$, as a function of the dimensionless lattice depth $s \equiv V_0/E_R$. The representative cases $s = 2$ and 20, indicated by vertical dashed lines, are considered in more detail in (b) and (c), respectively, which show the dimensionless chemical potential $\tilde{\mu}$ as a function of the quasi-momentum q in the first Brillouin zone (in units of π/d). The right panels display the location of the ^{87}Rb gap solitons considered in this work (points A–G).

are always expressed in terms of relevant dimensionless parameters, are valid for any BEC. Actually, this is a direct consequence of the scaling properties of Eqs. (1), (3), and (14).

A. Tight radial confinement: $E_R/\hbar\omega_{\perp} \ll 1$

In this case, the quantum of radial excitations is much greater than the typical energy scale in the linear problem. Note that, to realize this regime in the ^{87}Rb condensate, even in the OL of period $d \simeq 1.6 \mu\text{m}$, one needs to use the harmonic trap with radial frequency $\omega_{\perp}/2\pi \gtrsim 2400$ Hz.

Figure 1(a) shows the dimensionless chemical potential of the noninteracting 3D condensate with $E_R/\hbar\omega_{\perp} = 1/10$,

$$\tilde{\mu} \equiv (\mu - \hbar\omega_{\perp})/E_R, \quad (20)$$

as a function of the dimensionless lattice depth, $s \equiv V_0/E_R$. Since in this work we are interested in GSs with zero vorticity, this diagram, that represents the bandgap

structure of the underlying linear problem, has been obtained from the zero-vorticity solutions of the linear version of Eq. (17). Regions I, II, and III correspond to the lowest finite bandgaps, which separate shaded bands, where linear solutions exist. An important point is that, within the region of interest in the parameter space (for $V_0/E_R \lesssim 25$ and up to the third bandgap), this 3D diagram is indistinguishable from that obtained using the linear version of the effective 1D equation (18) [which, obviously, coincides with the linear version of the stationary 1D GPE (19)]. In fact, Eq. (18) leads to a bandgap diagram that differs from Fig. 1(a) solely in the band marked by the arrow, which does not appear in the 1D case. This extra band is, essentially, a replica of the lowest one, shifted up in energy by $2\hbar\omega_\perp/E_R$. Taking into account that the energy spectrum of the radial harmonic oscillator is given by

$$E = (2n_r + |m| + 1)\hbar\omega_\perp, \quad (21)$$

where $n_r = 0, 1, 2, \dots$ is the radial quantum number and $m = 0, \pm 1, \pm 2, \dots$ is the axial angular-momentum quantum number, it is evident that the additional up-shifted band corresponds to the first excited radial mode with $m = 0$. In the notation of Ref. [14], it corresponds to quantum numbers ($n = 1, m = 0, n_r = 1$), with n being the band index of the 1D axial problem. Thus, the appearance of this band is a purely 3D effect that cannot be accounted for by the above 1D models. Since the energy shift increases as $E_R/\hbar\omega_\perp$ decreases, it is clear that, within the parameter region of interest, Fig. 1(a) is universal in the sense that it is valid (for both 1D and 3D systems) for any $E_R/\hbar\omega_\perp \ll 1$.

In this work, we restrict ourselves to the case of $(1, 0, 0)$ GSs, that is, the solitons bifurcating from the lowest-energy band. Three-dimensional matter-wave GSs with a nontrivial radial structure have been studied in Ref. [14]. In this subsection, we consider OLs with $E_R/\hbar\omega_\perp = 1/10$ and depth $V_0/E_R = 2$ or 20 . These two representative cases correspond to the dashed vertical lines in Fig. 1(a) and are shown in more detail in Figs. 1(b) and (c), which display the corresponding bandgap structure as a function of the quasi-momentum in the first Brillouin zone (in units of π/d). Bold red lines in Figs. 1(b) and (c) have been obtained from the linear version of the effective 1D equation (18) while thin black lines correspond to those results obtained by means of the linear version of the 3D equation (17) that cannot be reproduced with the 1D model. As said above, the only appreciable difference between the 1D and 3D results comes from the contribution of the first excited radial mode [see the top part of Fig. 1(c)]. The case of $V_0/E_R = 2$, displayed in Fig. 1(b), corresponds to the condensate in relatively shallow OL potentials. Under these circumstances, the linear energy spectrum does not differ too much from that corresponding to the translationally invariant case ($V_z = 0$), and the bandgap structure exhibits wide energy bands separated by relatively small gaps, that are tangible only in the lowest part of the spectrum. On the contrary, for $V_0/E_R = 20$ (the tight-binding

regime) [see Fig. 1(c)] the condensate is trapped in the deep periodic potential. In this case, the lowest part of the linear spectrum is dominated by large gaps separating relatively narrow energy bands. The panels on the right side of Figs. 1(b) and (c) show the location, with respect to the corresponding linear bandgap diagram, of the GSs that will be considered below (points A–G). The horizontal axes in these panels indicate the number of atoms in each GS for the ^{87}Rb condensates (with the s -wave scattering length $a = 5.29$ nm) in the trap with radial frequency $\omega_\perp/2\pi = 2400$ Hz. For other values of parameters, the GS family is described by the same plots, if considered in terms of the above-mentioned nonlinear coupling constant, Na/a_\perp ($a = 5.29$ nm and $\omega_\perp/2\pi = 2400$ Hz correspond to $a/a_\perp = 0.024$). In other words, the number of atoms in a GS created in the condensate with scattering length a' and transverse confinement radius a'_\perp , which is tantamount to the GS with particular values of a , a_\perp and N , is given by

$$N' = \frac{aa'_\perp}{a'a_\perp}N. \quad (22)$$

GS solutions have been obtained by numerically solving the full 3D equation (17), as well as the effective 1D equations (18) and (19). To this end, we have implemented a *Newton continuation method*, based on a Laguerre–Fourier spectral basis, that uses the chemical potential μ as a continuation parameter. To ensure the convergence, methods of this kind require to initiate the iterative procedure with a sufficiently good initial guess. This means that one needs a good estimate for both the axial and the radial parts of the wave function. Our computations used the following initial ansatz for the wave function:

$$\psi_0(r_\perp, z) = \frac{1}{\Gamma a_\perp \sqrt{\pi}} \exp\left(-\frac{r_\perp^2}{2\Gamma^2 a_\perp^2}\right) \phi_0(z), \quad (23)$$

where the z -dependent condensate's width, expressed in units of a_\perp , is

$$\Gamma = (1 + 2aN|\phi_0(z)|^2)^{1/4}, \quad (24)$$

and $\phi_0(z) = \sqrt{k_0/2} \operatorname{sech}(k_0 z)$ is the axial wave function. The number of particles, N , and k_0 are free adjustable parameters. Note that the radial part of the wave function (23) is the same as the variational solution of Eq. (12), which was found in Ref. [17].

1. A shallow optical lattice: $V_0/E_R = 2$

Point A in Fig. 1(b) corresponds to a fundamental GS located near the bottom edge of the first bandgap. It looks qualitatively similar to that shown below in Fig. 3, but with the peak linear density $an_1(0) \simeq 0.04$. In this case, the effective 1D equations (18) and (19) yield results which are indistinguishable, on the scale of the figures, from those

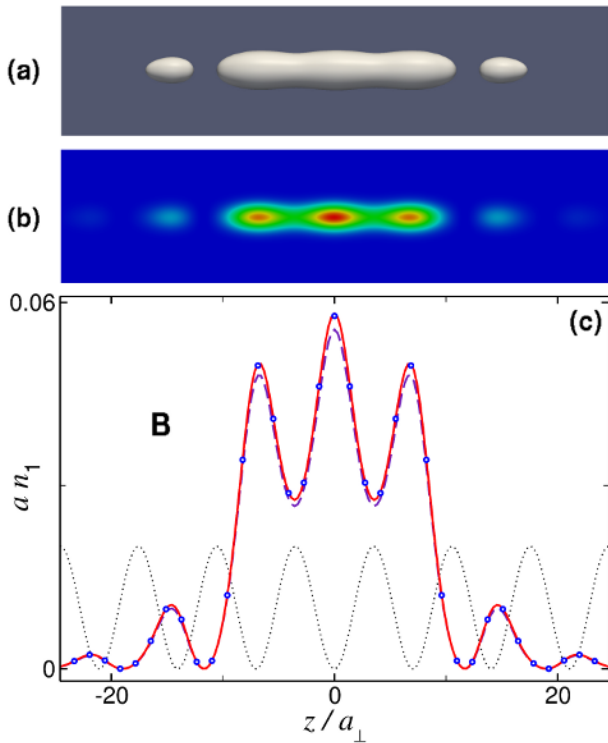


FIG. 2: (Color online). Atom density of the gap soliton corresponding to point B in Fig. 1(b), displayed as (a) an isosurface taken at 5% of the maximum density, and (b) as a color map along a cutting plane containing the z axis. (c) Dimensionless axial density an_1 obtained from the 3D wave function, as prescribed by Eq. (5) [open circles] along with the corresponding predictions from the nonpolynomial 1D equation (18) [solid red line] and the ordinary 1D GPE (19) [dashed blue line].

obtained from the full 3D equation (17). This is not surprising, as for these parameters condition (15) is certainly satisfied, and inequality $an_1 \ll 1$, which guarantees the validity of the 1D GPE (19), holds too. The (dimensionless) chemical potential of this GS is $\tilde{\mu} = 1.75$, which implies $\mu = 1.175 \hbar\omega_{\perp} \simeq \hbar\omega_{\perp}$, hence the radial wave function of the condensate should not differ too much from the ground state of the corresponding harmonic oscillator. These fundamental GSs, however, can only accommodate 9 particles (for the ^{87}Rb condensate), which is too small for the use of the mean-field approximation. Yet these solutions play an important role as building blocks of higher-order GSs. Point B in Fig. 1(b) corresponds to one of these higher-order solitons, which is built as a symmetric linear combination of three fundamental GSs, see Fig. 2. Its chemical potential and number of particles are $\tilde{\mu} = 1.75$ and $N = 35$. Note that, for the relatively shallow OL ($V_0/E_R = 2$), interference effects arising from the overlap between fundamental GSs sitting in adjacent lattice cells play an important role. For this reason, the contrast between the three central peaks and minima separating them

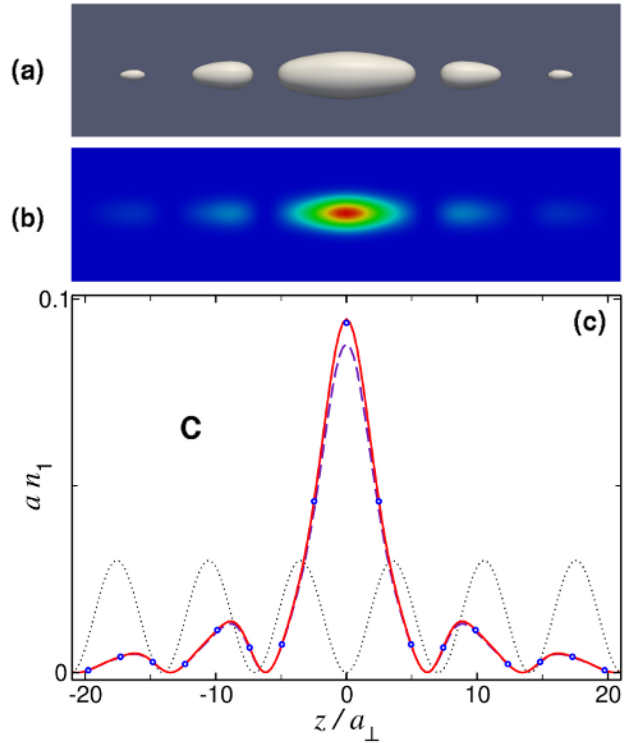


FIG. 3: (Color online). The same as Fig. 2 for the gap soliton corresponding to point C in Fig. 1(b).

is rather low in Fig. 2, and the total number of particles in the compound soliton does not coincide with the sum of the numbers of its fundamental constituents. Extending this procedure, one can readily build a sequence of compound GSs with an increasing number of peaks.

Panels (a) and (b) in Fig. 2, display the 3D density of the three-peak GSs – as, respectively, an isosurface (taken at 5% of the maximum density), and a color map in the cross-section plane drawn through the z axis. From these results, that have been obtained by solving the full 3D equation (17), we have also derived the axial linear density $n_1(z)$, defined as per Eq. (5). This density is shown in Fig. 2(c) by open circles, along with the corresponding results obtained from the effective 1D equations (18) and (19). The OL potential is also displayed by the dotted line (in arbitrary units). It is seen that the effective 1D equation (18) (solid red lines) reproduces the 3D results very accurately. The 1D GPE (19) (dashed blue lines) gives a slight discrepancy ($\simeq 3\%$) against the 3D results. This discrepancy, which would be invisible in the isolated fundamental GSs that build the compound, may also be explained by effects of the interference between the constituents.

Point C in Fig. 1(b) indicates the location of a fundamental gap soliton in the $(N, \tilde{\mu})$ plane, which sits near the top edge of the first bandgap. It contains 28 particles and has chemical potential $\tilde{\mu} = 2.42$, which corresponds to $\mu = 1.242 \hbar\omega_{\perp}$. This quantity is again very similar to

$\hbar\omega_{\perp}$, so that one expects the 1D GPE to be a good approximation in this case. Figure 3 shows the 3D density and the axial linear density $an_1(z)$ of this GS. In Fig. 3(c) one can see that the 1D GPE (19) (the dashed blue line) reproduces the 3D results obtained from the full GPE (17) (shown by open circles) within a 5% deviation. The effective 1D equation (18) (whose results are represented by the solid red line) is again more accurate and reproduces the 3D results with an error $< 1\%$. As before, this fundamental GS can be used to build multi-peak compounds.

As one moves upward in the bandgap, the 3D effects become stronger, which is a consequence of the fact that the corresponding number of particles and, thus, the nonlinear interaction energy increase. The above results, however, indicate that, for the tight radial confinement ($E_R/\hbar\omega_{\perp} \ll 1$) and shallow OL ($V_0/E_R \leq 2$), the specific 3D effects may be eventually neglected. In fact, under these conditions the maximum number of particles that can be accommodated in a fundamental GS in the first bandgap is so small that inequality $an_1 \ll 1$ always holds. This means that both the linear and the nonlinear energies remain much smaller than the quantum of the radial excitation (E_R , $an_1\hbar\omega_{\perp} \ll \hbar\omega_{\perp}$), hence no higher transversal modes are significantly excited. Therefore, the situation considered in this subsection may be categorized as the quasi-1D mean-field regime, in which the 1D GPE (19) accurately describes the matter-wave GSs, provided that condition $N \gg 1$ holds (otherwise, the mean-field approximation will be invalid).

2. A deep optical lattice: $V_0/E_R = 20$

In terms of the underlying OL, this is the case of the tight-binding regime, $V_0 \gg E_R$. The nonlinear tight-binding regime is realized when the potential depth V_0 is much larger than both the linear and nonlinear (mean-field) energies, i.e., $V_0 \gg E_R$, $an_1\hbar\omega_{\perp}$. Under these circumstances, the condensate density is highly localized near potential minima, making the overlap between densities associated with different wells negligible. Point D in the first bandgap of Fig. 1(c) corresponds to a fundamental GS with $\tilde{\mu} = 6.79$ and $N = 18$. Since its peak axial density is $an_1(0) \simeq 0.2$, and $V_0/E_R = 20$ implies $V_0 = 2\hbar\omega_{\perp}$, this fundamental GS belongs to the nonlinear tight-binding regime. Figure 4 shows a compound GS built of three such fundamental solitons. It corresponds to point E in Fig. 1(c). Its chemical potential, $\tilde{\mu} = 6.79$, is the same as that of the corresponding fundamental GS, and its number of particles, $N = 55$, now coincides with the sum of the number in its constituents (note that we always approximate N to the nearest integer). As can be seen from Fig. 4, this compound soliton exhibits three well separated identical peaks (BEC droplets), each one being practically indistinguishable from the above-mentioned fundamental GS. Figure 4(c) shows that the results obtained from the

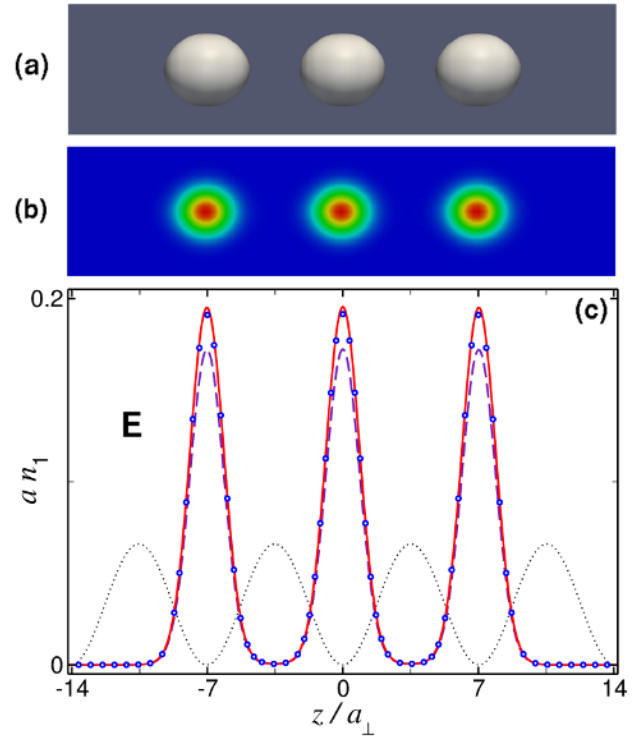


FIG. 4: (Color online). The same as Fig. 2 for the gap soliton corresponding to point E in Fig. 1(c).

effective 1D equation (18) (the solid red line) agree very well with those produced by the full 3D GPE (17) (open circles). In particular, the 1D equation yields the particle number $N = 56$, which is very close to $N = 55$, as given by the 3D solution. Since N represents a measurement of the norm of the wave function, it is clear that the error in the number of particles reflects the error in the corresponding wave functions. The 1D GPE (19), corresponding to the dashed blue line in Fig. 4(c), gives $N = 49$, which implies an error $\sim 10\%$.

Point F in Fig. 1(c) corresponds to a fundamental GS located near the top edge of the first bandgap. This soliton, which is very similar to that shown in Fig. 5, contains 71 particles and has chemical potential $\tilde{\mu} = 11.5$, which implies $\mu = 2.15\hbar\omega_{\perp}$. At this value of μ there is a significant probability of the excitation of higher levels in the radial-confinement potential, which is corroborated by the fact that the peak axial density of this GS is $an_1(0) \simeq 0.7$. Because inequality $an_1 \ll 1$ does not hold in this case, one cannot expect the ordinary 1D GPE (19) to be valid. In fact, it yields the number of particles $N = 53$, which implies an error greater than 25%. Nevertheless, the effective *nonpolynomial* 1D equation (18) remains *valid* and quite accurate. It produces $N = 73$, which corresponds to a maximum error of 2.8%. This is not surprising, since condition (15), which guarantees the validity of the nonpolynomial equation, is satisfied in this

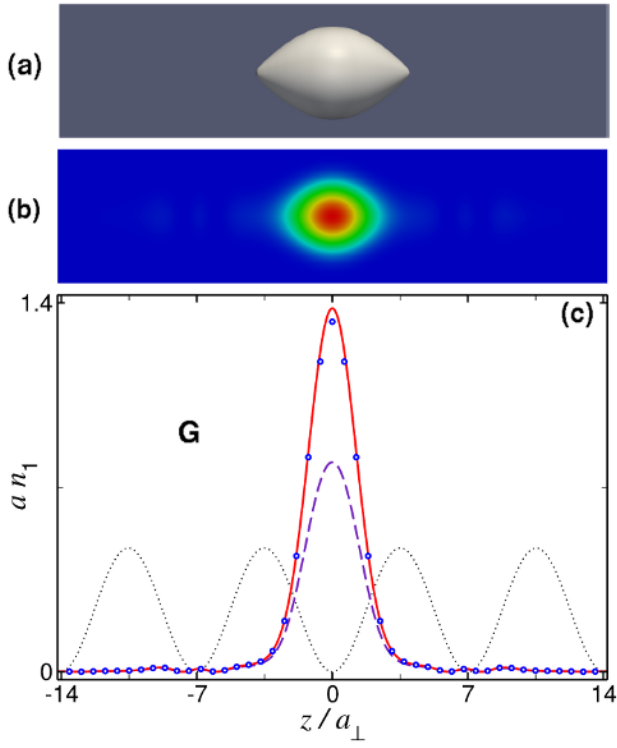


FIG. 5: (Color online). The same as Fig. 2 for the gap soliton corresponding to point G in Fig. 1(c).

case.

The solution pertaining to point G in Fig. 1(c) is qualitatively similar. It corresponds to the fundamental GS located near the top edge of the second bandgap, with chemical potential $\tilde{\mu} = 17.2$ and $N = 182$. Figure 5 shows the 3D density and axial linear density $an_1(z)$ of this BEC droplet. In this case, $an_1(0) \simeq 1.3$, indicating a large contribution of excited radial modes. As a consequence, the ordinary 1D GPE (19) [the dashed blue line in Fig. 5(c)] fails to reproduce the 3D results (open circles). It predicts $N = 119$, which means the error $> 34\%$. As seen from Fig. 5(c), the effective 1D equation (18) (the solid red line) remains accurate enough in this case too. In particular, it yields $N = 187$, the respective error being 2.8%.

The above results imply that, with the deep OL, the number of particles that can be accommodated in the fundamental GS can be large enough to make the 3D character of the wave function essential. In fact, even for the tight radial confinement ($E_R/\hbar\omega_\perp \ll 1$), which is the most favorable case for the applicability of the 1D approximation, the usual 1D GPE (19) with the deep OL potential cannot be reliably used beyond the first third of the first bandgap. Since the validity of the mean field treatment requires $N \gg 1$, the usual GPE cannot be used close to the bottom edge of the bandgap either. It is thus clear that the range of validity of this standard 1D equation is limited. This conclusion

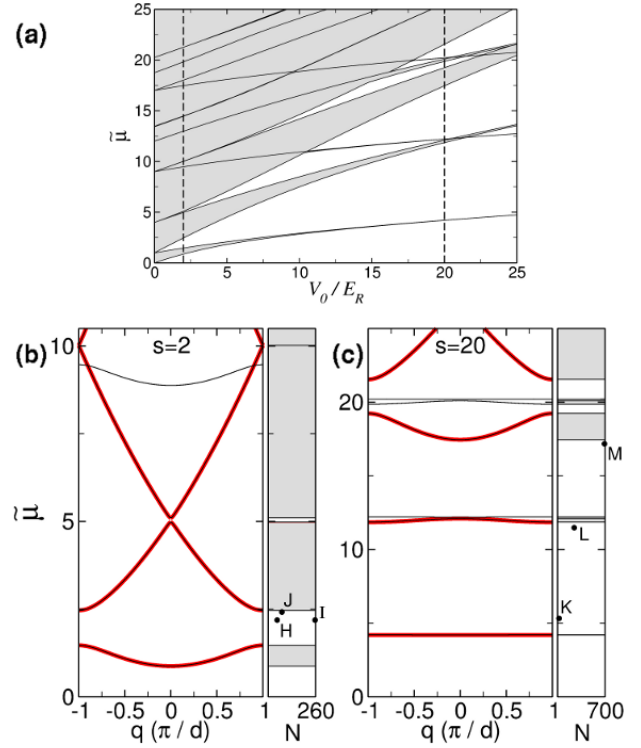


FIG. 6: (Color online). (a) Band-gap structure of a noninteracting 3D BEC with $E_R/\hbar\omega_\perp = 1/4$, as a function of the dimensionless lattice depth $s \equiv V_0/E_R$. The representative cases $s = 2$ and 20, indicated by vertical dashed lines, are considered in more detail in (b) and (c), respectively, which show the dimensionless chemical potential $\tilde{\mu}$ as a function of the quasi-momentum q in the first Brillouin zone (in units of π/d). The right panels display the location of the ^{87}Rb gap solitons considered in this work (points H–M).

becomes even more severe if one takes into account that the tight-radial-confinement regime is not easy to realize using typical experimental parameters. Our simulations indicate, however, that the effective nonpolynomial 1D equation (18) properly describes such essentially 3D situations, providing for an accurate description of the fundamental GSs in the entire bandgaps.

B. Intermediate radial confinement: $E_R/\hbar\omega_\perp \simeq 1/4$

This regime is of particular interest because it corresponds to typical experimental parameters. It can be realized, for instance, with the ^{87}Rb condensate in the OL of period $d = 1.55 \mu\text{m}$, radially confined by the harmonic potential with $\omega_\perp/2\pi = 960 \text{ Hz}$. The particle numbers N of the GSs considered below are given for these physical parameters, and, they can be converted into values of N for other situations by means of Eq. (22) (now, with $a/a_\perp = 0.015$).

Figure 6(a) shows the bandgap structure, as produced

by the linearized version of Eq. (17) for zero-vorticity modes. Recall that the linearization of the effective 1D equations (18) and (19) yield, instead, the diagram displayed on Fig. 1(a) (except for the narrow band marked by the arrow, which, as already said, does not appear in the 1D approximation). It is seen that the 1D approximation cannot reproduce the 3D picture resulting from the excitation of the radial modes, which manifest themselves in Fig. 6(a) as replicas of bands shifted up by integer multiples of $2\hbar\omega_{\perp}/E_R$. Since this quantity is smaller in the present case than it was before, the effect of these contributions in the region of interest is now stronger. While it is obvious that the 1D equations cannot account for the 3D effects originating from the shifted bands, we will demonstrate that these equations may still produce an accurate description of common GSs, i.e., those originating from the $m = n_r = 0$ energy bands.

Figures 6(b) and (c) display the bandgap structure as a function of the quasi-momentum for lattice depths $V_0/E_R = 2$ and 20, respectively. Thin black lines in these figures represent 3D results that cannot be reproduced by the 1D models, and points H–M in $(N, \tilde{\mu})$ plane mark examples of GSs that will be considered below.

1. A shallow optical lattice: $V_0/E_R = 2$

Point H in Fig. 6(b) corresponds to a fundamental GS with $\tilde{\mu} = 2.19$ and $N = 50$, which is similar to the one in Fig. 3, but with the peak axial density $an_1(0) \simeq 0.2$. In this case, the effective 1D equation (18) predicts $N = 51$, thus corresponding to a 2% error, while the 1D GPE (19) predicts $N = 45$ (an 11% error). Symmetric combinations of five such fundamental GSs generate the compound GS shown in Fig. 7, which contains 258 particles and corresponds to point I in Fig. 6(b). The 3D density of this soliton exhibits five weakly separated peaks, as shown in Figs. 7(a) and (b) by means of the isosurface and the color map in the cross-section plane drawn through the z axis. As seen in Fig. 7(c), in this case the effective 1D equation (18) yields an error of 1.5% in the norm of the wave function ($N = 262$) while the use of the ordinary 1D GPE (19) generates an error of 12% ($N = 226$), showing that, already for this GS, the 3D effects play an important role.

Point J in Fig. 6(b) corresponds to a fundamental GS containing 75 particles and located near the top edge of the first bandgap. It is qualitatively similar to the one shown in Fig. 3, but having $\tilde{\mu} = 2.42$ and $an_1(0) \simeq 0.26$. In this case, Eqs. (18) and (19) yield results with an error $\simeq 1\%$ ($N = 76$) and 12% ($N = 66$), respectively.

2. A deep optical lattice: $V_0/E_R = 20$

Points K, L and M in Fig. 6(c) correspond to fundamental GSs in the case of the tight-binding underlying linear

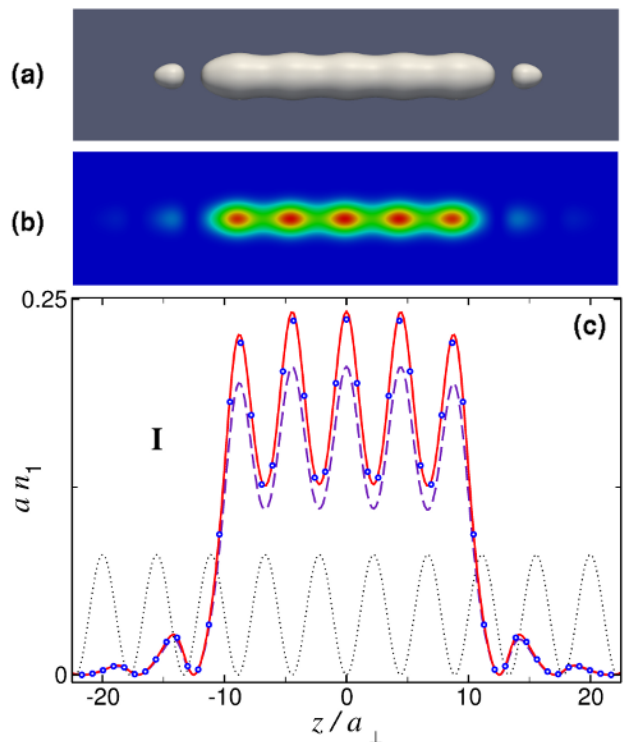


FIG. 7: (Color online). Atom density of the gap soliton corresponding to point I in Fig. 6(b), displayed as (a) an isosurface taken at 5% of the maximum density, and (b) as a color map along a cutting plane containing the z axis. (c) Dimensionless axial density an_1 obtained from the 3D wave function, as prescribed by Eq. (5) [open circles] along with the corresponding predictions from the nonpolynomial 1D equation (18) [solid red line] and the ordinary 1D GPE (19) [dashed blue line].

structure. The first soliton, which contains 19 particles, with $\tilde{\mu} = 5.33$ and axial density $an_1(0) \simeq 0.23$, also corresponds to the nonlinear tight-binding regime and is thus highly localized at a single lattice site. This follows from the fact that, for $V_0/E_R = 20$ and $E_R/\hbar\omega_{\perp} = 1/4$, one has $V_0/\hbar\omega_{\perp} = 5$, which is much greater than the above-mentioned value of $an_1(0)$. For this GS, located near the bottom edge of the first bandgap, the ordinary 1D GPE (19) yields an error $> 11\%$, which continues to grow as one moves upward in the bandgap. However, the effective nonpolynomial 1D equation (18) remains accurate within a 2.5% deviation.

Point L in Fig. 6(c) indicates the position of a fundamental GS near the top edge of the first bandgap, with $\tilde{\mu} = 11.5$, $N = 243$, and $an_1(0) \simeq 2.3$. Since the inequality $an_1 \ll 1$ does not hold in this case, the ordinary 1D GPE (19) is invalid, giving a 45% error ($N = 133$). Note that, even though point L is relatively close to a 3D energy band [the thin black line in Fig. 6(c)], which cannot be reproduced by the effective 1D equation (18), it can, however, reproduce this GS within a 4% error ($N = 253$).

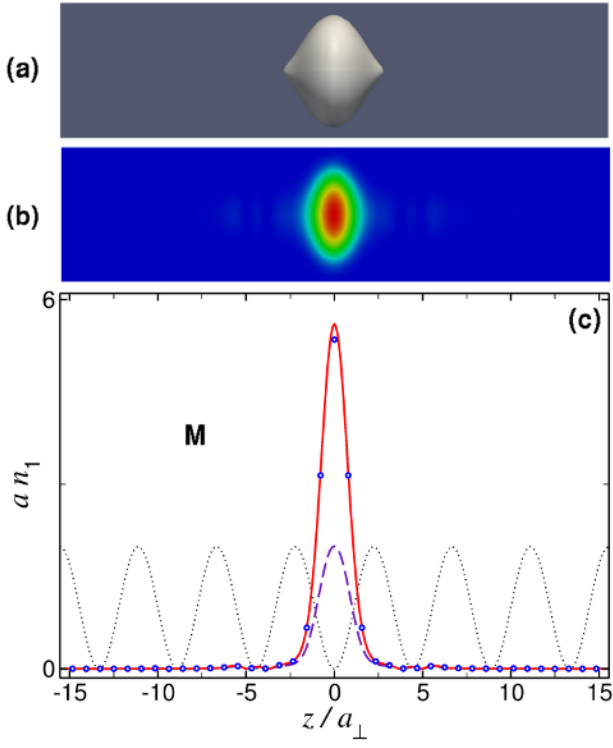


FIG. 8: (Color online). The same as Fig. 7 for the gap soliton corresponding to point M in Fig. 6(c).

The same is true for the fundamental GS displayed in Fig. 8, which corresponds to point M in Fig. 6(c). It represents a BEC droplet containing 696 particles, with $\tilde{\mu} = 17.2$ and the peak axial density $an_1(0) \simeq 5.4$. Since we have $V_0/\hbar\omega_\perp < an_1(0)$ in the present case, the system is no longer in the nonlinear tight-binding regime. This is seen in Fig. 8, where the density is not strongly localized around the minimum of the potential well. As seen in Fig. 8(c), the nonpolynomial 1D equation (18) yields results (the solid red line) that agree with the 3D picture produced by the full GPE (17) (open circles), within a 3% deviation [Eq. (18) yields $N = 719$ in this case]. On the contrary, the 1D GPE (19), which gives results (the dashed blue line) with an error $> 55\%$ (it yields $N = 297$), clearly is not valid in this case.

These findings demonstrate that, in the physically relevant regime of the intermediate radial confinement ($E_R/\hbar\omega_\perp \gtrsim 1/4$), even for the shallow OL the 3D effects may be important, and thus the usual 1D GPE (19) fails to reproduce correctly the axial density $an_1(z)$ and the particle content N . For $E_R/\hbar\omega_\perp = 1/4$ and potential depth $V_0/E_R = 2$, the fundamental GSs located in the first bandgap, as predicted by the 1D GPE equation, feature the error $\simeq 12\%$, which is still larger for compound GSs. For the deep OL ($V_0/E_R = 20$), the 1D GPE is valid only in a small region near the bottom edge of the first bandgap. In general, this equation is applicable only

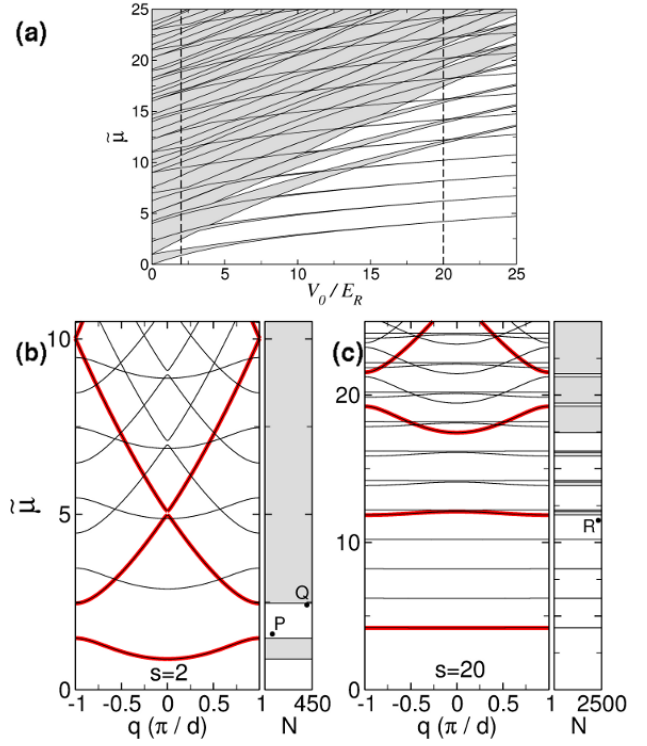


FIG. 9: (Color online). (a) Band-gap structure of a noninteracting 3D BEC with $E_R/\hbar\omega_\perp = 1$, as a function of the dimensionless lattice depth $s \equiv V_0/E_R$. The representative cases $s = 2$ and 20 , indicated by vertical dashed lines, are considered in more detail in (b) and (c), respectively, which show the dimensionless chemical potential $\tilde{\mu}$ as a function of the quasi-momentum q in the first Brillouin zone (in units of π/d). The right panels display the location of the ^{87}Rb gap solitons considered in this work (points P–R).

where both conditions $an_1 \ll 1$ and $N \gg 1$ hold simultaneously. As $E_R/\hbar\omega_\perp$ increases, the relative strength of the radial confinement decreases, and the range of validity of the 1D GPE becomes more and more narrow. From the experimental viewpoint, the increase of $E_R/\hbar\omega_\perp$ may be relevant, as in this way one can easily increase the number of particles in the fundamental GSs. However, the increase of $E_R/\hbar\omega_\perp$ also implies a decrease in the relative size of the radial-excitation energy quantum, which can compromise the stability of the solitons because they can decay by exciting higher radial modes, even for condensates with a relatively small number of particles. We briefly consider this case below. The stability properties of the GSs will be analyzed in Sec. IV.

C. Weak radial confinement: $E_R/\hbar\omega_\perp \geq 1$

In this regime, the typical energy scale in the underlying linear problem is sufficiently large to easily excite higher transverse modes. As a representative example, we con-

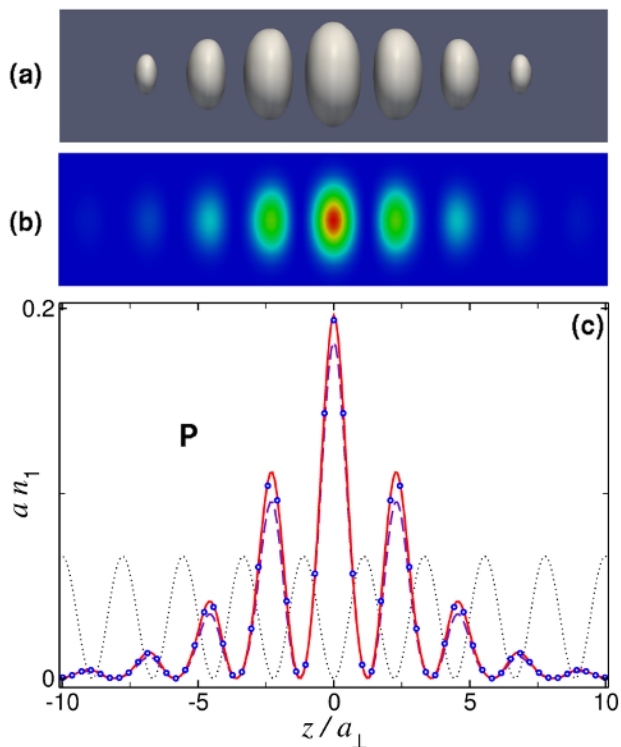


FIG. 10: (Color online). Atom density of the gap soliton corresponding to point P in Fig. 9(b), displayed as (a) an isosurface taken at 5% of the maximum density, and (b) as a color map along a cutting plane containing the z axis. (c) Dimensionless axial density an_1 obtained from the 3D wave function, as prescribed by Eq. (5) [open circles] along with the corresponding predictions from the nonpolynomial 1D equation (18) [solid red line] and the ordinary 1D GPE (19) [dashed blue line].

sider the case of $E_R/\hbar\omega_{\perp} = 1$, which can be realized in the ^{87}Rb condensate in the OL with $d = 1.55 \mu\text{m}$ and radial-confinement strength $\omega_{\perp}/2\pi = 240 \text{ Hz}$. The particle contents of the GSs considered below correspond to such condensates. As before, the corresponding values of N can be converted into those corresponding to other situations by means of Eq. (22) (this time, $a/a_{\perp} = 7.6 \times 10^{-3}$).

Figure 9(a) displays the bandgap structure of the underlying 3D linear problem, to be compared with Fig. 1(a) which shows the bandgap structure obtained from the linearization of 1D equations (18) or (19). As before, the latter equations cannot account for the 3D contributions from the excited radial modes, which account for the series of shifted bands separated by gaps of value $2\hbar\omega_{\perp}/E_R$ in Fig. 9(a). Figures 9(b) and (c) display the linear bandgap structure as a function of the quasi-momentum, for $V_0/E_R = 2$ and 20, respectively.

Point P in Fig. 9(b) corresponds to a fundamental GS with $\tilde{\mu} = 1.59$ and $N = 74$. Its 3D density plot, shown in Fig. 10, demonstrates that this fundamental soliton is spread over several lattice sites, which is a consequence of

the fact that its chemical potential is very close to the first linear energy band, where only extended solutions of the stationary GPE exist. Figure 10(c) shows that the results obtained from the effective 1D equation (18) (the solid red line) coincide with the 3D results (open circles) within 1% (it predicts $N = 75$). However, the 1D GPE (19) (the dashed blue line) gives rise to an error $\simeq 10\%$ (it predicts $N = 66$). We thus conclude that, in the weak-radial-confinement regime ($E_R/\hbar\omega_{\perp} \geq 1$), the latter equation is only applicable in a narrow region close to the bottom edge of the first bandgap, even for shallow OLs. In this regime, the 3D contributions play an important role in most cases. These contributions are, however, well accounted for by the effective 1D equation (18). For instance, for point Q in Fig. 9(b) [which corresponds to a fundamental GS near the top edge of the first bandgap, with $\tilde{\mu} = 2.42$, $N = 400$, and $an_1(0) \simeq 1.5$] the 1D GPE (19) gives an error of 34% ($N = 265$), while the nonpolynomial 1D equation (18) limits the error to 3.5% ($N = 414$). Point R in Fig. 9(c) is an example of a fundamental GS in a deep OL. It corresponds to a disk-shaped BEC droplet trapped in a single lattice cell [see Fig. 11(b)], which contains 2323 ^{87}Rb atoms, and has $\tilde{\mu} = 11.5$. Its axial linear density is qualitatively similar to that shown in Fig. 8(c), but with a maximum value $an_1(0) \simeq 23$. In this case, the 1D GPE predicts the particle content $N = 534$, while the effective 1D equation (18) yields $N = 2437$, which corresponds to an error $\simeq 5\%$ in the norm of the wave function. Thus, the 1D nonpolynomial equation provides for a sufficiently good description of the stationary GSs even in the highly nonlinear ($an_1 \gg 1$) weak-radial-confinement regime.

IV. STABILITY ANALYSIS

We have investigated the stability of the GS solutions by monitoring their long-time behavior after the application of a random perturbation [13, 29]. Specifically, we have perturbed the corresponding wave functions with a small-amplitude ($\sim 2\%$) additive Gaussian white noise and have monitored the subsequent nonlinear evolution for 1 s. To this end we have numerically solved the full 3D GPE (1), as well as the effective 1D equation (14), using a Laguerre-Fourier pseudospectral method with a third-order Adams-Bashforth time-marching scheme. Numerical integration of the 3D GPE for such a long time is a very demanding computational task. While it is possible for a certain GS to be metastable and decay on a time scale still longer than 1 s, in practice this time is long enough in comparison with the lifetime of the condensate per se, hence the soliton surviving for 1 s may be categorized as a stable one.

We have found that both the full 3D GPE (1) and the effective nonpolynomial 1D equation (14) lead to the same conclusions regarding the stability of the GSs. However, once an unstable soliton begins to decay, one cannot expect, in general, the latter equation to reproduce the dy-

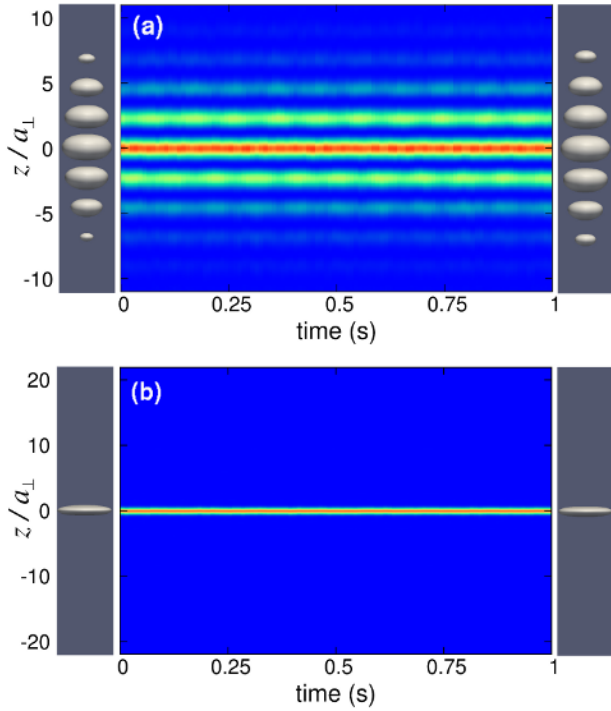


FIG. 11: (Color online). Evolution in time, after the application of a 2% white-noise perturbation, of the fundamental gap solitons corresponding (a) to point P in Fig. 9(b), and (b) to point R in Fig. 9(c).

namical behavior correctly. The reason for this problem is that, as already said in Sec. II, in the presence of the OL potential the above-mentioned adiabatic condition (i) is hard to fulfill in time-dependent settings. Of course, the same is true for the 1D equation (3), which is a limit form of Eq. (14) and, consequently, has a much narrower range of applicability. The results presented below have been obtained using the full 3D GPE (1). For each GS we have used at least two different basis sets and time steps to check that the results do not depend on details of the numerical procedure.

Our simulations demonstrate that, in general, $(1, 0, 0)$ fundamental GSs are stable, except in a narrow region close to the top edge of the bandgaps. In particular, the solitons corresponding to points A, D, K, and P in Figs. 1, 6, and 9 remain stable up to $t = 1$ s. On the contrary, GSs in a shallow OL ($V_0/E_R = 2$), located close to the top edge of a bandgap, such as those corresponding to points C, H, J, and Q in Figs. 1, 6, and 9, turn out to be unstable. This instability manifests itself as a steady decay of the norm of the GS through emission of radiation, on a time scale that increases as one moves away from the top edge of the bandgap. In this regard, one finds that the GS corresponding to point H decays much slower than the other ones. As the lattice depth V_0/E_R increases, in general, GSs become more stable and the instability region shrinks. In particular,

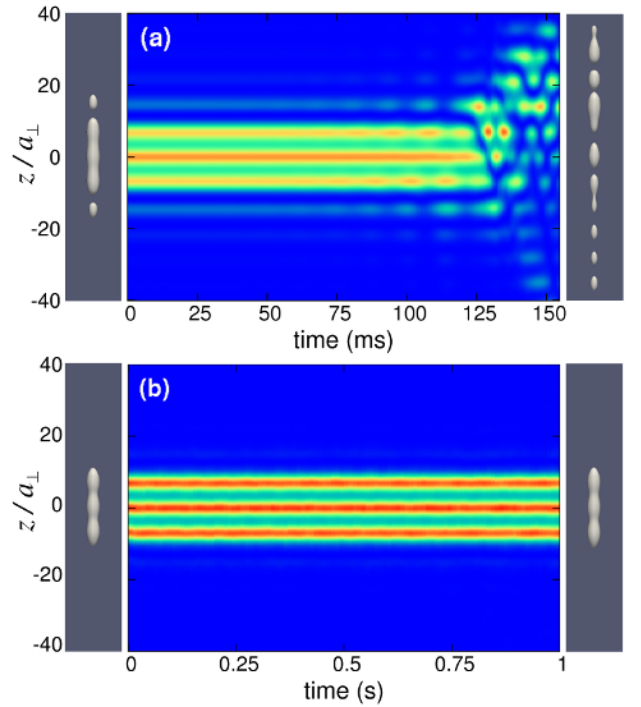


FIG. 12: (Color online). (a) Evolution in time, after the application of a 2% white-noise perturbation, of the compound gap soliton corresponding to point B in Fig. 1(b). Panel (b) displays the long time behavior, after the application of the perturbation, of a stable three-peak soliton (see text).

our simulations indicate that GSs such as those corresponding to points F, G, L, M and R in Figs. 1, 6, and 9 (which are fundamental GSs in the deep OL, with $V_0/E_R = 20$, located close to the top edge of the bandgap) also remain stable up to $t = 1$ s. This is in good agreement with previous analyzes carried out in the context of deep optical lattices in terms of the ordinary 1D GPE (3) [9, 13].

An important result is that $(1, 0, 0)$ fundamental GSs remain stable even in the weak-radial-confinement regime ($E_R/\hbar\omega_\perp \simeq 1$). In this regime, GSs always have sufficient energy to excite higher radial modes, and, as a consequence, the 3D effects are always relevant and the usual 1D GPE (3) fails. Figure 11(a) displays the long-time behavior, after the application of the perturbation, of the fundamental GS shown in Fig. 10 [it corresponds to point P in Fig. 9(b)]. This figure shows (by means of a color map) the evolution of the axial density $an_1(z, t)$, which has been obtained from the 3D wave function $\psi(\mathbf{r}_\perp, z, t)$ by integrating out the radial dependence, as per Eq. (5). The left panel in this figure shows the 3D condensate density at $t = 0$ (i.e., just after the application of the perturbation) as an isosurface taken at 5% of the maximum density, while the right panel represents the density at $t = 1$ s. This GS has $\tilde{\mu} = 1.59$, which implies $\mu = 2.59\hbar\omega_\perp$. Note that, despite the fact that this chemical potential is greater

than the quantum $\hbar\omega_{\perp}$, the GS remains stable up to 1 s. The same is true for the fundamental GS corresponding to point R in Fig. 9(c), which corresponds to a disk-shaped BEC containing more than 2300 ^{87}Rb atoms with chemical potential $\mu = 12.5\hbar\omega_{\perp} \gg \hbar\omega_{\perp}$. As Fig. 11(b) shows, this GS also remains stable.

Our simulations also demonstrate that the compound GS from Fig. 2, corresponding to point B in Fig. 1(b), is unstable. This is seen in Fig. 12(a), which shows how the soliton decays on a time scale $\simeq 120$ ms after the addition of a 2% white-noise perturbation. This compound GS, which have $\tilde{\mu} = 1.75$ and $N = 35$, was built in the shallow OL ($V_0/E_R = 2$) as the symmetric combination of three fundamental constituents. We have found that, in such shallow lattices, GSs of this type are always unstable. However, it is not difficult to find stable solitons of this type in somewhat deeper lattices. An example is shown in Fig. 12(b), which represents a stable three-peak soliton with $\tilde{\mu} = 3.13$ and $N = 59$, trapped in the OL with $V_0/E_R = 4$ and $E_R/\hbar\omega_{\perp} = 1/10$. Similar dynamics is observed for the GS displayed in Fig. 7, which corresponds to point I in Fig. 6(b). This is a five-peak compound generated in the shallow OL ($V_0/E_R = 2$) in the regime of the intermediate radial-confinement strength ($E_R/\hbar\omega_{\perp} \simeq 1/4$). Our simulations indicate that this compound soliton is unstable. In fact, no stable five-peak solitons were found in such a shallow lattice. On the other hand, it is not difficult to find stable compounds of this kind for deeper OLs. An example is the five-peak pattern with $V_0/E_R = 4$, $E_R/\hbar\omega_{\perp} = 1/4$, $\tilde{\mu} = 2.83$ and $N = 212$. In general, GSs naturally become more stable as the lattice depth increases. For deep OLs ($V_0/E_R = 20$), the stability of compound GSs is essentially identical to that of their fundamental constituents. The GS in Fig. 4, which corresponds to point E in Fig. 1(c), is an example of a stable three-peak soliton realized in a deep OL.

V. CONCLUSIONS

To appraise the physical relevance of the results reported in this work, it is pertinent to recall that the mean-field treatment of the GSs (gap solitons), based on the GPE, is valid if $N \gg 1$ and the condensate is sufficiently dilute so that $a^3\bar{n} \ll 1$, where a is the scattering length of the interatomic collisions, and \bar{n} is the atomic density. In shallow OLs (optical lattices) such conditions can be easily met, though the former one imposes a serious limitation on the range of applicability of the usual 1D GPE (19), which fails as N increases. In deep OLs, where the tunneling between adjacent cells is strongly suppressed, the above conditions must be fulfilled at each site of the lattice. Under these circumstances, GSs may have a rather high local density. A good estimate for the 3D peak density $n(\mathbf{0}) = N|\psi(\mathbf{0})|^2$ in terms of the peak axial density, $n_1(0)$, can be obtained

from the following relation [17]:

$$n(\mathbf{0}) = \frac{n_1(0)}{\pi a_{\perp}^2 \sqrt{1 + 4an_1(0)}}. \quad (25)$$

Substituting the values of $an_1(0)$ obtained in Section III for different GSs into Eq. (25), one can easily verify that condition $a^3n(\mathbf{0}) \ll 1$ is satisfied in all cases, which justifies the use of the mean-field description. The most critical situation occurs for the GS corresponding to point G in Fig. 1(c), which has $a^3n(\mathbf{0}) \simeq 10^{-4}$. For the GS corresponding to point R in Fig. 9(c), one finds $a^3n(\mathbf{0}) \simeq 5 \times 10^{-5}$.

Despite the fact that applicability conditions for the mean-field treatment can be readily met, it is much harder to justify the validity of the usual 1D GPE (3), which requires *both* conditions $an_1 \ll 1$ and $N \gg 1$ to be hold simultaneously. Only in this case the 3D effects may be safely neglected. In most experimentally relevant situations, these conditions are not met, hence the applicability range of Eq. (3) turns out to be very limited. On the contrary, it has been shown in this work that the effective 1D GPE (14) with the nonpolynomial nonlinearity provides for an accurate description of the stationary matter-wave GSs in most cases of practical interest.

A relevant extension of the present analysis may be to GSs with intrinsic vorticity, as well as to mobility of stable solitons. It is also interesting to consider two-component GSs in the realistic 3D setting.

V.D. acknowledges financial support from Ministerio de Ciencia e Innovación through contract No. FIS2009-07890 (Spain).

* Electronic address: ammateo@ull.es

† Electronic address: vdelgado@ull.es

‡ Electronic address: malomed@post.tau.ac.il

- [1] V. A. Brazhnyi and V. V. Konotop, *Mod. Phys. Lett. B* **18**, 627 (2004).
- [2] O. Morsch and M. Oberthaler, *Rev. Mod. Phys.* **78**, 179 (2006).
- [3] R. Carretero-González, D. J. Frantzeskakis, and P. G. Kevrekidis, *Nonlinearity* **21**, R139 (2008).
- [4] P. G. Kevrekidis, D. J. Frantzeskakis, and R. Carretero-González (editors), *Emergent Nonlinear Phenomena in Bose-Einstein Condensates: Theory and Experiment* (Springer, Heidelberg, Germany, 2007).
- [5] Y. V. Kartashov, B. A. Malomed, and L. Torner, *Solitons in nonlinear lattices*, *Rev. Mod. Phys.*, in press.
- [6] E. P. Gross, *Nuovo Cimento* **20**, 454 (1961); *J. Math. Phys.* **4**, 195 (1963); L. P. Pitaevskii, *Zh. Eksp. Teor. Fiz.* **40**, 646 (1961) [*Sov. Phys. JETP* **13**, 451 (1961)].
- [7] A. Muñoz Mateo and V. Delgado, *Phys. Rev. Lett.* **97**, 180409 (2006).
- [8] J. A. M. Huhtamäki, M. Möttönen, T. Isoshima, V. Pietilä, and S. M. M. Virtanen, *Phys. Rev. Lett.* **97**, 110406 (2006).
- [9] P. J. Y. Louis, E. A. Ostrovskaya, C. M. Savage, and Y. S. Kivshar, *Phys. Rev. A* **67**, 013602 (2003).

- [10] F. Kh. Abdullaev and M. Salerno, Phys. Rev. A **72**, 033617 (2005).
- [11] T. Maytevarunyoo and B. A. Malomed, Phys. Rev. A **74**, 033616 (2006).
- [12] Y. Zhang and B. Wu, Phys. Rev. Lett. **102**, 093905 (2009).
- [13] Y. Zhang, Z. Liang, and B. Wu, Phys. Rev. A **80**, 063815 (2009).
- [14] A. Muñoz Mateo, V. Delgado, and B. A. Malomed, Phys. Rev. A **82**, 053606 (2010).
- [15] A. E. Muryshev, G. V. Shlyapnikov, W. Ertmer, K. Sengstock, and M. Lewenstein, Phys. Rev. Lett. **89**, 110401 (2002).
- [16] L. Salasnich, A. Parola, and L. Reatto, Phys. Rev. A **65**, 043614 (2002); L. Salasnich, Laser Phys. **12**, 198 (2002).
- [17] A. Muñoz Mateo and V. Delgado, Phys. Rev. A **77**, 013617 (2008); Phys. Rev. A **75**, 063610 (2007); Ann. Phys. (N.Y.) **324**, 709 (2009).
- [18] S. Middelkamp, G. Theocharis, P. G. Kevrekidis, D. J. Frantzeskakis, and P. Schmelcher, Phys. Rev. A **81**, 053618 (2010).
- [19] G. Theocharis, A. Weller, J. P. Ronzheimer, C. Gross, M. K. Oberthaler, P. G. Kevrekidis, and D. J. Frantzeskakis, Phys. Rev. A **81**, 063604 (2010).
- [20] C. Wang, P. G. Kevrekidis, T. P. Horikis, D. J. Frantzeskakis, Phys. Lett. A, **374**, 3863 (2010).
- [21] S. Middelkamp, J. J. Chang, C. Hamner, R. Carretero-González, P. G. Kevrekidis, V. Achilleos, D. J. Frantzeskakis, P. Schmelcher, and P. Engels, Phys. Lett. A **375**, 642 (2011).
- [22] An independent derivation of this formula was reported by F. Gerbier, Europhys. Lett. **66**, 771 (2004).
- [23] L. Salasnich, B.A. Malomed, and F. Toigo, Phys. Rev. A **76**, 063614 (2007).
- [24] A. Muñoz Mateo and V. Delgado, Phys. Rev. A **74**, 065602 (2006).
- [25] S. Adhikari and B.A. Malomed, Europhys. Lett. **79**, 50003 (2007); Physica D **238**, 1402 (2009).
- [26] F. H. Mies, E. Tiesinga, and P. S. Julienne, Phys. Rev. A **61**, 022721 (2000).
- [27] B. Eiermann, Th. Anker, M. Albiez, M. Taglieber, P. Treutlein, K.-P. Marzlin, and M. K. Oberthaler, Phys. Rev. Lett. **92**, 230401 (2004).
- [28] J. Armijo, T. Jacquemin, K. Kheruntsyan, and I. Bouchoule, Phys. Rev. A **83**, 021605(R) (2011).
- [29] J. Yang and Z. H. Musslimani, Opt. Lett. **28**, 2094 (2003).